

A Study on the Reconstruction of Moderate Contrast Targets Using the Distorted Born Iterative Method

Roberto Lavarello, *Student Member, IEEE*, and Michael Oelze, *Member, IEEE*

Abstract—Previous tomographic methods using ultrasound for reconstructing sound speed and attenuation images suffered from convergence issues for targets with moderate speed of sound contrast. Convergence problems can be overcome by the use of the multiple frequency, distorted Born iterative method (DBIM). The implementation of DBIM for measurement configurations in which receiver positions are fixed was studied, and a novel regularization scheme was developed. The regularization parameter needed to stabilize the inversion process initially was found through the Rayleigh quotient iteration, then relaxed according to the relative residual error between the measured and estimated scattered fields. The DBIM was successfully stabilized for both full and partial receiver angular coverage without a significant loss in spatial resolution. The effects of variable density in the reconstructions were briefly explored through simulations. The ability to reconstruct targets with moderate contrast was validated through experimental measurements. Speed of sound profiles for balloons filled with saline in a background of water were reconstructed using multiple frequency DBIM techniques. The mean squared error for speed of sound reconstructions of the balloon phantoms with 16.4% sound speed contrast was 1.1%.

I. INTRODUCTION

ACOUSTICAL imaging techniques have been used extensively for many applications since as early as the development of sonar in the 1910s. One of the most widely used techniques based on the sonar principle is known as B-mode imaging [1], which has applications in nondestructive evaluation and medical imaging. B-mode images are qualitative representations of the changes in the acoustic impedance function, which allows some differentiation among different media. Spatial resolution on the order of a wavelength can be obtained with the use of arrays [2] and highly focused single element transducers. Even though the image quality can deteriorate due to phase and amplitude aberrations [3], the image formation process is both simple and reliable.

The measured acoustic waves, however, carry much more information than is exploited in B-mode imaging. When an incident acoustic wave encounters an inhomogeneity, it is scattered in every direction. The scattered

wave is a function of the shape and acoustic properties of the inhomogeneity. The inverse scattering problem consists of estimating the distribution of acoustic parameters (i.e., sound speed, acoustic attenuation, and density) given a set of measurements of the scattered field. From the distribution of acoustic parameters estimated through inverse scattering, tomograms of the scattering object can be constructed. This technique allows a more detailed description of the imaging target because parameters other than the acoustic impedance can be imaged. Furthermore, unlike B-mode imaging, which provides qualitative information about the object being interrogated, the solution to the inverse scattering problem is quantitative and related to the mechanical properties of the object.

Despite its advantages, acoustic inverse scattering has not been nearly as successful as other tomographic imaging modalities such as X-ray tomography, nuclear tomography (SPECT and PET), and magnetic resonance imaging (MRI) [4]. One of the reasons is the lack of applications that can successfully exploit the unique features of inverse scattering in acoustics. Currently, the main application of acoustic inverse scattering has been the imaging of the female breast for the detection of cancer [5]–[7]. Ultrasonic computed tomography devices have been built for lower frequency ultrasound (less than 3 MHz) with resolutions on the order of a few millimeters [8], [9]. However, the contrast mechanism between benign and malignant masses in breast tissue has not yet been identified. Some works argue that the speed of sound is the main contrast mechanism [10], but many researchers have found a stronger differentiation on the acoustic attenuation, for which B-mode imaging is insensitive [8], [11]. However, even for moderate signal-to-noise ratios (SNRs), the attenuation images are of lower quality than the speed of sound images [12]. Most likely, the contrast mechanism depends on more than one parameter.

Another problem of inverse scattering techniques is the lack of computational techniques that are both robust and efficient. The first algorithms, developed in the early 1970s, were based on the projection theory used in X-ray and nuclear tomographic techniques. These algorithms were used to reconstruct maps of speed of sound [13] and attenuation [14]. However, unlike other tomographic methods, straight line propagation is not a realistic model for ultrasonic wave propagation in biological media because of refraction and diffraction effects. Therefore, these techniques had only a limited success.

Manuscript received March 29, 2007; accepted August 8, 2007. This work was supported in part by a grant from the 3M Corporation.

The authors are with the Department of Electrical and Computer Engineering, University of Illinois at Urbana-Champaign, Urbana, IL 61801 (e-mail: lavarell@uiuc.edu).

Digital Object Identifier 10.1109/TUFFC.2008.621

Diffraction tomography then was developed, which is based on first order approximations to the wave equation using either the Born [15] or Rytov [16] approximations. Despite its computational efficiency and mathematical elegance, diffraction tomography is limited because the quality of the reconstructions degrades severely, even for moderate values of sound speed contrast Δc , i.e., moderate changes in the speed of sound of target from background [17], [18]. More recent algorithms solve for the full wave equation without resorting to single scattering approximations. Newton-based approaches in frequency domain were studied during the 1990s [19], [20], but they suffer from two well-known problems. First, these methods can have convergence issues [21], which can be addressed by the use of multiple frequencies or frequency hopping [22]. Second, these methods are computationally expensive. The method of moments (MoM) is commonly used to discretize the integral wave equation, which requires the inversion of large, nonsparse matrices. More recently, alternative inverse scattering methods with lower computational cost [23], [24] have been proposed, but they have yet to be extensively tested. Therefore, reliable inverse scattering techniques are not yet suitable for applications such as real-time breast imaging because of their computational cost. In contrast, pulse-echo imaging techniques such as B-mode allow for real-time image formation.

In summary, inverse scattering techniques have reached a certain level of maturity that has not been exploited so far in applications that can take advantage of its unique features. Currently, the use of inverse scattering techniques for breast imaging has met with success, but it has yet to become widely accepted by clinicians as a diagnostic tool. Promising applications for this technology exist at higher ultrasonic frequencies (larger than 20 MHz). For example, a high-frequency, ultrasound-computed tomography (HFUS-CT) device could be used to image the mechanical properties of small samples of native or bioengineered tissues under different biomechanical stresses. Such a device could have significant impact on functional tissue engineering. Similarly, a HFUS-CT device could be used to image the mechanical properties of large cells for the construction of models of scattering from cells at conventional ultrasonic frequencies.

The purpose of this paper is to develop techniques for implementing the distorted Born iterative method (DBIM) [19] for HFUS-CT applications and to validate experimentally the ability to reconstruct objects with moderately large Δc . Several issues are discussed throughout the present work. An overview of DBIM for negligible changes in density is presented in Section II. The implementation of DBIM for measurement configurations in which the receiver positions are fixed, and a method for the selection of the regularization parameter needed to stabilize the inversion process based on the Rayleigh quotient iteration are presented in Section III. Simulation results, including the effect of density changes in the reconstructions and an experimental validation of the algorithms are presented in Section IV. Conclusions are presented in Section V.

II. THE DISTORTED BORN ITERATIVE METHOD

The goal of inverse scattering methods is to extract acoustic parameters of an object from a set of measurements of the scattered field. The relationship between the acoustic pressure and the acoustic parameters in an inhomogeneous medium is given by the Helmholtz equation:

$$\nabla \cdot \varrho^{-1}(\vec{\rho}) \nabla p(\vec{\rho}) + \omega^2 \kappa(\vec{\rho}) p(\vec{\rho}) = -\phi^{\text{inc}}(\vec{\rho}), \quad (1)$$

where ϱ and κ are the density and compressibility, respectively, p is the acoustical pressure, ω is the angular frequency, ϕ^{inc} are the acoustical sources, and $\vec{\rho}$ is the position vector. The solution to (1) can be represented in terms of the Green's function $G_r(\vec{\rho})$ corresponding to a background with density $\varrho_r(\vec{\rho})$ and compressibility $\kappa_r(\vec{\rho})$. For the case when the changes in density are negligible, the inhomogeneities of the medium can be represented by the wave number function $k = \omega/c$, in which ω is the angular frequency and $c = 1/\sqrt{\kappa\varrho}$ is the speed of sound. The wave equation can be written in integral form as:

$$p(\vec{\rho}, k) = p^{\text{inc}, k_r}(\vec{\rho}) + \int_{\Omega} d\vec{\rho}' [k^2(\vec{\rho}') - k_r^2(\vec{\rho}')] p(\vec{\rho}', k) G_r(\vec{\rho}, \vec{\rho}'), \quad (2)$$

where the notation $p(\vec{\rho}, k)$ represents the acoustic pressure when the wave number function is $k(\vec{\rho})$, $p^{\text{inc}, k_r}(\vec{\rho})$ is the incident acoustic field when the background is $k_r(\vec{\rho})$, and Ω is the space region occupied by the object to be imaged. Eq. (2) will be referred to as the forward solver equation. If a reference k_r with a known associated Green's function G_r is chosen, the forward solver equation can be used to calculate $p(\vec{\rho}, k)$, $\vec{\rho} \in \Omega$ if $k(\vec{\rho})$ is known. The most common choice for the reference is a uniform background k_0 , for which the Green's function is proportional to the zeroth-order Hankel function of the second kind $H_0^{(2)}(k_0\rho)$ or to $\exp(-ik_0r)/r$ for two-dimensional and three-dimensional spaces, respectively. Other choices can be used for more specialized problems, such as imaging in layered media [25]. The forward solver equation also can be used to calculate the pressure at any point outside Ω , once the pressure field has been calculated for all $\vec{\rho} \in \Omega$. Because the Green's function satisfies the same differential equation as the pressure field, the forward solver can be used to numerically calculate the Green's function for an arbitrary reference background.

The reciprocal of the forward solver is to find $k(\vec{\rho})$ from a set of measurements of the acoustic field $p(\vec{\rho}, k)$ outside the scatterer. However, if $k(\vec{\rho})$ is not known, the integral equation (2) cannot be used because $p(\vec{\rho}, k)$, $\vec{\rho} \in \Omega$ also is unknown. Using a reference background $k_b(\vec{\rho})$ with corresponding Green's function $G_b(\vec{\rho}, \vec{\rho}')$, and by invoking the first-order Born approximation $p(\vec{\rho}, k) \approx p^{\text{inc}, k_b}(\vec{\rho}) = p(\vec{\rho}, k_b)$, results in:

$$p(\vec{\rho}, k) - p(\vec{\rho}, k_b) \approx \int_{\Omega} d\vec{\rho}' [k^2(\vec{\rho}') - k_b^2(\vec{\rho}')] p(\vec{\rho}', k_b) G_b(\vec{\rho}, \vec{\rho}'). \quad (3)$$

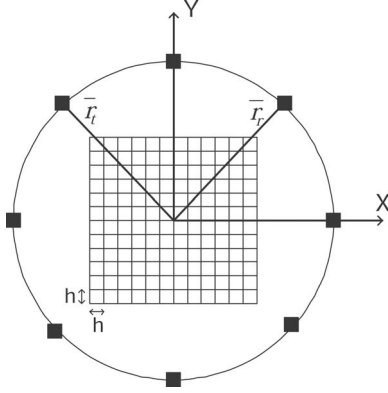


Fig. 1. Schematic of the configuration used for the scattered data measurement.

Eq. (3) will be referred to as the inverse solver equation. For the chosen profile $k_b(\vec{\rho})$, both $p(\vec{\rho}, k_b)$ and $G_b(\vec{\rho}, \vec{\rho}')$ can be calculated using the forward solver, and the only unknown in (3) is the wave number function. However, because the inverse solver equation is just an approximation, the obtained solution will not be exact. The DBIM [19] is a Newton-type approach that solves the inverse scattering problem by iteratively refining an initial guess $k_b(\vec{\rho})$ using the forward solver to predict the pressure field and the inverse solver to correct the guessed wave number profile. The termination criterion depends on the relative residual error (RRE), defined as:

$$\text{RRE} = \frac{\|p(\vec{\rho}, k) - p(\vec{\rho}, k_b)\|}{\|p(\vec{\rho}, k)\|}. \quad (4)$$

The process continues until the RRE falls below the noise floor. Continuing beyond this point will cause the left-hand side of (3) to be driven by noise and the solution using DBIM to diverge [19].

III. COMPUTATIONAL ISSUES IN THE IMPLEMENTATION OF THE DBIM

A. Forward and Inverse Scattering Solvers

The region of interest encompassing the object to be reconstructed is centered at the origin of a two-dimensional space and discretized using N square pixels of side h . The number of transmitters and receivers are represented by N_t and N_r , respectively. For the present work, the transmitters and receivers are placed on the same locations over a circle of radius R , as shown in Fig. 1.

The MoM using sinc basis functions and delta testing functions [26] is used to discretize the integral equations. The resulting matrix equations for the forward and inverse solvers are quite different in behavior. The forward solver matrix is square and well-conditioned because both the nonradiating sources and the testing points lie inside the integration volume. The forward solver matrix is commonly inverted using Krylov subspace methods such as the

biconjugate gradient stabilized (BiCGSTAB) [27] in combination with fast Fourier transform (FFT) algorithms to perform the matrix-vector multiplications [28]. This technique has a computational cost of $O(N_t N \log N)$ and a storage requirement of $O(N_t N)$.

In contrast, the inverse solver matrix is ill-conditioned because the testing points are outside the integration volume and, therefore, away from the nonradiating sources. In order to improve the conditioning of the matrix, there must be enough diversity in the pressure field measurements. The diversity can come from the spatial distribution of the transmitters and receivers, and/or from the use of multiple frequency data. FFT-based solvers are not applicable because the transmitter/receivers are not placed on a uniform grid. Therefore, one has to resort to inversion methods such as the conjugate gradient applied to the normal equations (CG-NR). The computational cost and memory requirement of the CG-NR solver are both $O(N_t N_r N)$. The memory requirement is too large, even for small sized problems, which makes it the main drawback of the full-matrix implementation of the inverse solver.

An alternative approach can be used for any sampling configuration for which the receiver positions are held constant for all transmitter positions [29], such as the one shown in Fig. 1. This formulation will be referred to as the reduced-matrix approach. For these cases, the inverse solver matrix can be decomposed as N_t decoupled matrix equations, each one in the form:

$$\{h^2 \mathbf{G} \text{diag}(\mathbf{f}_i^{\text{int}})\} \mathbf{o} = \mathbf{e}^i, \quad (5)$$

where \mathbf{G} is a N_r by N matrix with each row representing the discretized Green's function corresponding to $k_b(\vec{\rho})$, $\mathbf{f}_i^{\text{int}}$ is the i -th column of the N by N_t matrix \mathbf{F}^{int} representing the acoustic field inside each pixel per each transmitter position, $\text{diag}(\cdot)$ denotes a diagonal matrix with the argument on its main diagonal, \mathbf{e}^i is a vector of length N_r corresponding to the error between the predicted and measured pressure field when the transmitter is at the i -th position, and \mathbf{o} is a vector of length N corresponding to the unknown object function $[k^2(\vec{\rho}) - k_b^2(\vec{\rho})]$. If the inverse solver matrix is denoted by \mathbf{M} , both the operations $\mathbf{y} = \mathbf{M}\mathbf{x}$ and $\mathbf{y} = \mathbf{M}^H \mathbf{x}$ can be performed operating block by block, which leads to a reduced memory requirement of $O([N_t + N_r]N)$. The computational complexity is the same as for the full-matrix solver.

Matrix-free approaches [20], [30] also have been used in order to avoid the formation of the inverse solver matrix. These algorithms are based on the fact that the direct and Hermitian multiplication by \mathbf{M} can be cast as wave propagation and backpropagation problems, respectively. Therefore, these operations can be computed using the same class of algorithms as for the forward solver. When implemented on a single node, the computational cost is of $O(C_1 N_t N \log N + C_2 N_t N_r N)$ with C_1, C_2 multiplicative constants. As a result, the computational cost is larger than for the full and reduced-matrix approaches. The memory requirement, as in the reduced-matrix approach, is $O((N_t + N_r)N)$.

Both the reduced-matrix and matrix-free approaches can be parallelized easily on a single node. However, when distributed on N_n nodes, the matrix-free approach also can reduce the amount of memory per each node by a factor of N_n with a minimum volume of data to be transmitted along nodes and only a slight overhead in execution time to allow for node communication [31]. The reduced-matrix approach does not share these benefits. Additionally, the computational cost of the reduced-matrix approach is much higher than the one of the matrix-free approach if the receivers are not fixed for every experiment, because this implies that several Green's function matrices \mathbf{G} need to be calculated.

B. Use of Frequency Hopping

The main limitation of frequency domain inverse scattering methods is that they diverge when the contrast in the wave number function is above a certain threshold [21]. The divergence condition is called the phase wrapping effect. It occurs approximately when $\Delta\phi > \pi$, where $\Delta\phi$ represents the excess phase that the incident field accumulates when traveling through the scatterer if refraction effects are neglected. The frequency hopping method [20], [22], [32] can be used to overcome the divergence limitation for objects with moderate-to-large Δc . This method consists of solving the inverse problem first with a frequency low enough so that the phase wrapping effect is avoided. To improve the spatial resolution, the low-frequency solution is used as starting guess for another DBIM reconstruction using a higher frequency.

C. Proposed Regularization Scheme

The inverse solver is stabilized with the use of Tikhonov regularization [33], which consists of solving the optimization problem

$$\hat{\mathbf{o}} = \underset{\mathbf{o}}{\arg \min} \{ \|\mathbf{e} - \mathbf{M}\mathbf{o}\|_2^2 + \alpha \|\mathbf{o}\|_2^2 \}, \quad (6)$$

where \mathbf{M} is the inverse solver matrix and α is the regularization parameter. The effect of Tikhonov regularization is to modify the singular values of the inverse solver matrix. If the singular values of \mathbf{M} are denoted by σ_i , applying Tikhonov regularization is equivalent to filtering the contribution of σ_i to the reconstructed image using:

$$H(\sigma_i) = \frac{\sigma_i^2}{\sigma_i^2 + \alpha}. \quad (7)$$

Contributions from $\sigma_i^2 \gg \alpha$ will remain unchanged, but the ones from $\sigma_i^2 \ll \alpha$ will be removed from the reconstructed image. Therefore, choosing an appropriate value for α is a very important issue when regularizing the inverse solver.

Several methods to determine the optimum α for linear matrix equations are available in the literature, such as the L-curve [34] or the generalized cross validation (GCV) [35].

However, the applicability of these methods is warranted mainly because of two reasons. First, in order to determine the optimum α value, both GCV and the L-curve methods involve solving (6) several times using different α values, and, therefore, these techniques are computationally expensive. Second, and more important, choosing the regularization parameter using these methods may have a detrimental effect on the convergence of DBIM. The L-curve method will be used to exemplify this assertion. Eq. (6) was solved for values of $\alpha = 10^\beta$, with $\beta \in [-23, -9]$. For reference, the square of the dominant singular value of the matrices \mathbf{M} was on average around 10^{-11} . In order to form the L-curve, (6) is solved by inverting the regularized pseudo-inverse $(\mathbf{M}^H\mathbf{M} + \alpha\mathbf{I})$ using Gaussian elimination. The CG-NR method is not used to solve (6) because the typical shape of the L-curve is not achieved unless a very large number of iterations is used due to the self-regularizing properties of the method [36]. This is yet another limitation of the use of the L-curve for the selection of α .

Fig. 2 shows the L-curves corresponding to the third DBIM iteration of the reconstruction of circular cylinders with radius 2.4λ and speed of sound contrasts of 4% and 10%, which correspond to $\Delta\phi$ values of 0.369π and 0.873π , respectively. The first case converges to an RRE of 5% at the fourth iteration with a root mean square error (RMSE) of 20.84%. The regularization parameter for all iterations was chosen as the one that maximized the curvature of the corresponding L-curves. For all iterations, the L-curves showed a smooth shape similar to the one in Fig. 2(a). The second case, however, diverges from the true solution even though $\Delta\phi < \pi$. The RMSE at the third iteration is 286.21%, and even further, the shape of the L-curve is not well defined, which makes it impossible to determine a proper value of α for the following iterations. This is due to the fact that deviations from the true solution are due to not only random noise in the scattered pressure data, but also mostly from inaccuracies in (3) due to the Born approximation, which becomes more significant when the speed of sound contrast increases.

Some other approaches to find α can be found in the literature. Haddadin and Ebbini [37] used a truncated singular value decomposition (SVD) approach to regularize the inverse solver. However, SVDs are very expensive to calculate. Furthermore, even for moderate-sized problems \mathbf{M} is too large to be constructed, which compromises the calculation of its SVD. Liu [38] used 1% of the first diagonal element of the matrix $\mathbf{M}^H\mathbf{M}$ as the regularization parameter. Franchois and Pichot [39] proposed an approach that related the regularization parameter to a monomial function of the RRE. This scheme depended on two parameters that were empirically determined. Wang *et al.* [40] devised a heuristic rule using two parameters: an initial regularization parameter between 0.1 and 10, and a contraction factor between 1.25 and 5. Even though these schemes relate α to properties of \mathbf{M} , it is not clear how these choices relate to the SVD of \mathbf{M} . Furthermore, these choices of α depend on selecting values for independent

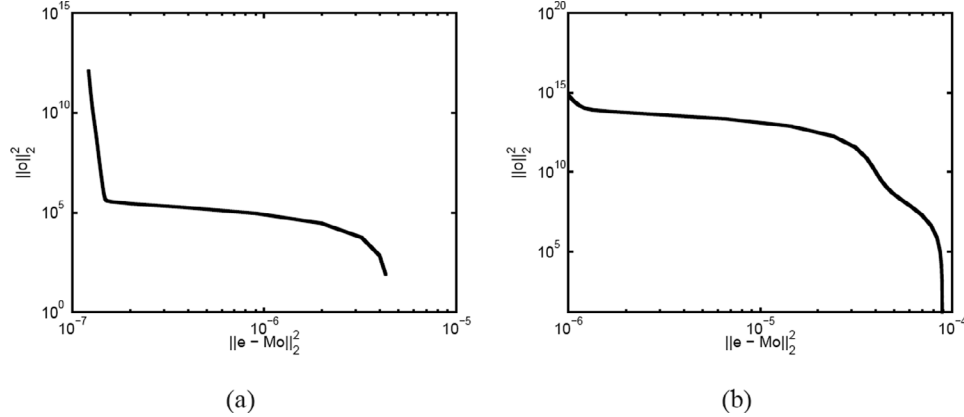


Fig. 2. L-curves corresponding to the third iteration of the DBIM reconstruction of circular cylinders with 2.4λ radius and speed of sound contrasts equal to (a) 4% and (b) 10%.

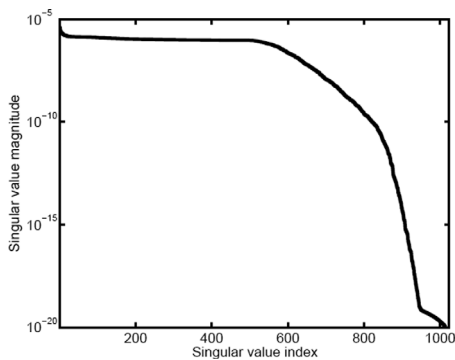


Fig. 3. SVD of the inverse solver matrix using $k_b = k_0$, a 32 by 32 grid with pixel size $\lambda/5$, and full angular coverage. A total of 46 line transmitters/receivers are placed at a distance 300λ from the center of the discretization grid, as shown in Fig. 1.

parameters, and it is unclear how to properly choose them for different scanning configurations. Therefore, a systematic and yet efficient approach to select the regularization parameter needs to be developed.

If no a priori information is available, the initial guess for the profile $k_b(\vec{\rho})$ usually is chosen to be k_0 , which is equivalent to using diffraction tomography. The SVD of the inverse solver matrix corresponding to this choice of $k_b(\vec{\rho})$ is shown in Fig. 3. In fact, the structure of the SVD of the matrix \mathbf{M} does not change significantly during the DBIM process. When the measurements are performed deep in the farfield, the maximum spatial resolution of inverse scattering methods is constrained to 0.3536λ – 0.5λ [41]. This agrees with the typical SVD curve shown in Fig. 3, which is highly uniform for all singular values that correspond to frequencies below the spatial resolution threshold.

The initial regularization parameter α is chosen to be comparable to the square of the first singular value σ_0 of the inverse solver matrix. This choice is sufficient to avoid rapid variations in the initial reconstructed profiles, which have been found to be critical to the convergence of inverse scattering algorithms [39]. As the RRE decreases, the value of the regularization parameter can be relaxed to

TABLE I
REGULARIZATION PARAMETER SELECTION SCHEME AS A FUNCTION OF THE FORWARD ERROR.

| RRE | Regularization parameter α |
|------------------------------|-----------------------------------|
| $0.5 < \text{RRE}$ | $\sigma_0^2/2$ |
| $0.25 < \text{RRE} \leq 0.5$ | $\sigma_0^2/20$ |
| $\text{RRE} \leq 0.25$ | $\sigma_0^2/200$ |

allow for contributions from higher frequencies. Because of simplicity, the relaxation process used in this work is based on RRE thresholding. The proposed scheme is shown in Table I.

In order to apply the regularization parameter selection scheme, one has to estimate the value of σ_0 . This task was performed using the Rayleigh quotient iteration [42]. This technique only requires matrix-vector multiplication operations, which can be calculated using either the matrix-free or reduced-matrix formulations. Furthermore, this method does not require the explicit formation of the inverse solver matrix. For all cases analyzed in the present work, less than eight iterations were required to converge to the actual value of σ_0 with a precision of 0.001%.

IV. RESULTS

A. Single Frequency DBIM Simulations with Synthetic Data

The reconstruction algorithm and regularization method were tested first through simulations. For compliance with previous works [21], the inversion method was tested with analytic scattered data generated for infinite-circular cylinders [43], using n by n grids with $n = 32, 64, 128,$ and 256 . The scattered data were contaminated using 5% Gaussian noise ($\text{SNR} = 26$ dB). For all the simulations in the present work, the number of transmitter/receivers was chosen so that $N_t = N_r = \sqrt{2N}$, and $h = \lambda/5$. The radii of the cylinders were $2.4\lambda, 5\lambda, 10\lambda,$ and 22λ , respec-

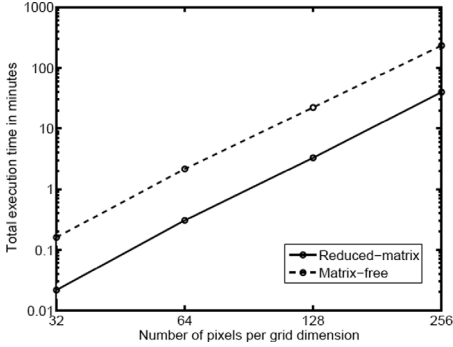


Fig. 4. Execution time in minutes of the DBIM algorithm when using as a function of the number of pixels per grid dimension.

tively. The speed of sound contrasts were 11%, 5%, 2.5%, and 1.1%, respectively. These values were chosen so that $\Delta\phi \approx 0.95\pi$, so no frequency hopping was required to perform the inversions. The DBIM execution time in a dual-processor Opteron 248 computer (AMD, Sunnyvale, CA) with 4 GB of memory, using both the reduced-matrix and matrix-free approaches, is shown in Fig. 4.

For all cases, nine DBIM iterations were required to complete the reconstructions, and the RMSE in the reconstruction of the wave number function was about 12%. These results verify the scalability of the regularization scheme, which does not alter the performance when reconstructing equivalent targets in terms of $\Delta\phi$ for different grid sizes. None of the reconstructions diverged even though the $\Delta\phi$ value was larger than the ones used in Section III-C for the L-curve analysis. For a complete comparison with the L-curve results, a 2.4λ radius cylinder with $\Delta c = 4\%$ also was reconstructed using the proposed regularization scheme. The RRE dropped below 5% at the fifth iteration with an RMSE of 16.32%. Therefore, even though the inversion required one additional iteration, the error using the proposed method is lower than the one obtained with α chosen by the L-curve.

As expected, the computational performance of the reduced-matrix implementation is somewhat better than for the matrix-free algorithm. The execution time improvement factor was approximately 7.5 for the 32 by 32 grid, and it decreased to 5.8 for the 256 by 256 grid. As expected, the improvement factor decreased slowly as the number of unknowns increased. Therefore, even for a single node implementation, the performance gain provided by the reduced-matrix approach over the matrix-free algorithm was not too significant.

B. Frequency Hopping Reconstructions with Synthetic Data

Frequency hopping simulations were performed using a phantom target similar to the one used by Haddadin and Ebbini [32]. The phantom was constructed using homogeneous cylinders with different centers, radii, and speed of sound contrasts. The specifications of the phantom are given in Table II. The maximum $\Delta\phi$ when using frequencies of 1 and 2 MHz are 1.07π and 2.14π , respectively.

TABLE II
SPECIFICATIONS OF THE PHANTOM USED FOR THE FREQUENCY HOPPING SIMULATIONS.¹

| Cylinder number | Center position | Radius | Speed of sound contrast |
|-----------------|-----------------------------|--|-------------------------|
| 1 | [0,0] | 10λ (outer) 10.6λ (inner) | 5.5% |
| 2 | [0,0] | 10λ | 3.9% |
| 3 | $[-3.4\lambda, 3.4\lambda]$ | 3.4λ | 6% |
| 4 | $[3.4\lambda, -3.4\lambda]$ | 3.4λ | 6% |
| 5 | $[-5\lambda, -5\lambda]$ | 0.4λ | 0.6% |
| 6 | $[5\lambda, 5\lambda]$ | 0.2λ | 0.6% |

¹The dimensions are given in terms of the wavelength λ at 2 MHz.

Fig. 5(a) shows the ideal speed of sound contrast distribution. Fig. 5(b) shows the result of applying single frequency DBIM at 2 MHz, for which the algorithm diverges as expected. Even though the reconstruction has some qualitative value (i.e., the positions and radii of the cylinders have been identified correctly), it completely lacks quantitative value. The range of sound speed values for all cylinders is incorrect. Negative speed of sound contrast values have been reconstructed even though the contrast in the actual profile is always positive. Fig. 5(c) shows a reconstruction at 1 MHz terminated when the RRE dropped below 25%. In the presence of noise, if the low frequency reconstruction is terminated when $\text{RRE} \approx \text{SNR}$, the initial residual for the high-frequency iterations is close to the noise floor and resolving the finer resolution features of the image becomes difficult. Fig. 5(d) shows the reconstruction at 2 MHz using Fig. 5(c) as initial guess. The reconstruction was terminated when $\text{RRE} \approx \text{SNR}$. The RMSE in the speed of sound reconstruction was 0.4% (Δc RMSE = 9%), and the two inclusions with size smaller than a wavelength were recovered, which suggests that the reconstructed profile has both numerical accuracy and good spatial resolution. Therefore, the proposed regularization scheme effectively stabilizes the inversion without severely degrading the quality of the reconstructions.

C. Effect of Density Variations

A common assumption in inverse scattering studies is that density variations are negligible. However, the contrast mechanism in soft tissues is not completely understood, which suggests that actual contributions to inverse scattering from density variations may not be negligible. Therefore, the effect of density variations in reconstructions using the DBIM algorithm need to be considered.

To examine the effects of density variations on inverse scattering, consider the case of a homogeneous scatterer embedded in a homogeneous background. The background has acoustic parameters κ_0 , ρ_0 , and k_0 . The scatterer has constant acoustic parameters κ , ρ , and k . The integral wave equation in complete form can be written as:

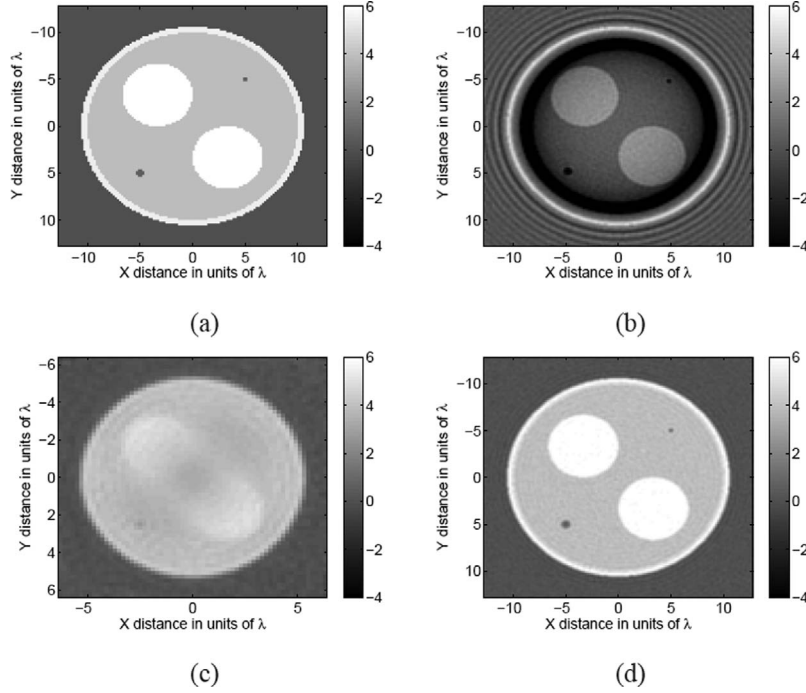


Fig. 5. Reconstruction of phantom target using frequency hopping. (a) Ideal speed of sound contrast distribution. (b) Single frequency reconstruction at 2 MHz. (c) Single frequency reconstruction at 1 MHz. (d) Frequency hopping reconstruction at 2 MHz using (c) as initial guess.

$$p^{\text{sc}}(\vec{\rho}, k) = \int_{\Omega} d\vec{\rho}' [k^2 - k_0^2] p(\vec{\rho}') G_0(\vec{\rho}, \vec{\rho}') + \int_{\Omega} d\vec{\rho}' [\nabla \gamma_{\rho}(\vec{\rho}') \cdot \nabla p(\vec{\rho}')] G_0(\vec{\rho}, \vec{\rho}'), \quad (8)$$

where $\gamma_{\rho} = \frac{\rho_0}{\rho} - 1$ and $p^{\text{sc}}(\vec{\rho}, k) = p(\vec{\rho}, k) - p^{\text{inc}, k_0}(\vec{\rho})$. The only difference between (2) and (8) is the integral involving the divergence of the density. Therefore, for scatterers with piecewise constant density, the effect of neglecting density variations when reconstructing the wave number distribution will be localized around the discontinuities in ρ .

Simulations were performed to evaluate the effects of changes in density for piecewise homogeneous scatterers. The simulated targets were two circular symmetric cylinders. The scattered data was generated using the analytical solution for cylindrical wave illumination. The derivation of the expression for the scattered field is described in the Appendix. The speed of sound contrasts and diameters were set to 4% and 10.4λ for the outer cylinder, and 6% and 5.2λ for the inner cylinder, respectively. This corresponds to a maximum phase change of approximately 0.99π . The results for several density variation distributions are presented in Fig. 6. No noise was included in the simulated scattered data in order to isolate the effect of the changes in density. The reconstructions were truncated when the RRE dropped below 1%. Fig. 6(a) is a reconstruction when there are no variations in density, and it is shown as a reference. The reconstruction follows the ideal contrast profile very closely, with some minor ringing at the edges of the cylinders. Fig. 6(b) corresponds to density variations equal to the corresponding

speed of sound contrasts inside each cylinder, i.e., 4% in the outer cylinder and 6% in the inner one. The edges of the cylinders appear more distorted than the ones shown in Fig. 6(a). Some minor fluctuations appear away from the edges. Fig. 6(c) corresponds to density variations equal to four times the corresponding speed of sound contrasts inside each cylinder, i.e., 16% in the outer cylinder and 24% in the inner one. As expected, the reconstruction appears more distorted than in the previous two cases. However, the mean value of the speed of sound inside each cylinder has been correctly determined. Fig. 6(d) corresponds to density variations equal to four times the speed of sound contrast of the first cylinder for both cylinders, i.e., 16% on both cylinders. The inner cylinder is reconstructed with minimal distortion because there are no density variations between the inner and outer cylinders. The edges of the outer cylinder, however, appear distorted as in Fig. 6(c). These simulations verify the fact that, for piecewise constant density distributions, the effect of density changes is localized at the density discontinuities and does not largely affect the speed of sound reconstructions if the density changes are comparable to the speed of sound changes and the scatterer is large compared to the acoustic wavelength.

Neglecting density changes can have a large impact on the reconstruction of acoustic impedance. The estimated acoustic impedance contrasts are 4% and 6% for the cases shown in Fig. 6(b)–(d) because the density contrast is assumed to be 0%. But the true acoustic impedance contrast values are approximately 8% and 12%, 20% and 31%, and 20% and 23%, respectively. Therefore, in order to construct a more accurate acoustic impedance model, density vari-

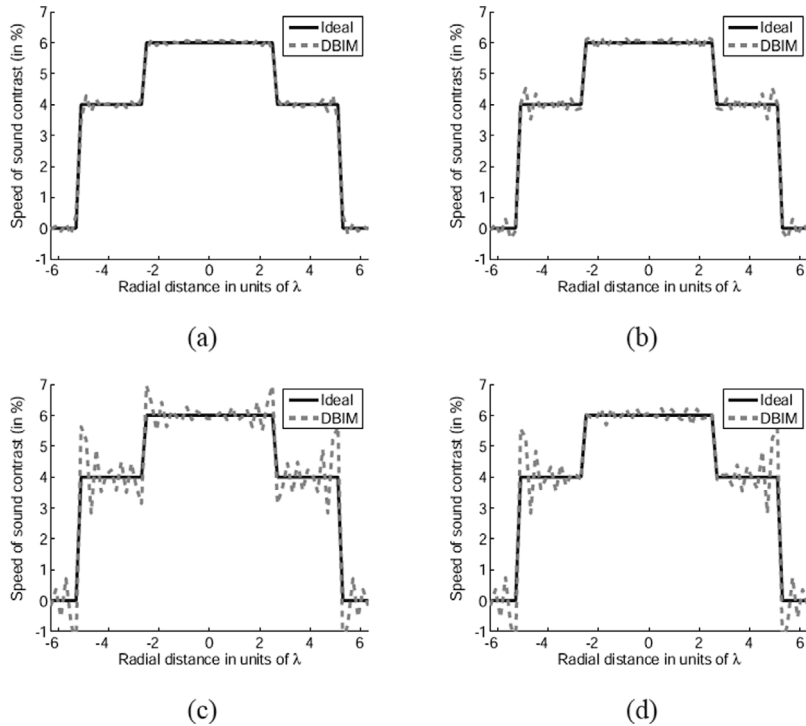


Fig. 6. DBIM reconstructions when the inversion algorithm neglects changes in density. The speed of sound contrasts and diameters are 4% and 10.4λ for the outer cylinder, and 6% and 5.2λ for the inner cylinder, respectively. The density contrasts were set equal to (a) 0% for both cylinders. (b) The corresponding speed of sound contrasts inside each cylinder. (c) Four times the corresponding speed of sound contrasts inside each cylinder. (d) Four times the speed of sound contrast of the outer cylinder for both cylinders.

ations may need to be considered. Some studies of the numerical solution to the variable density wave equation are available in the literature [44]–[46].

D. Experimental Results

Experiments were conducted to validate the ability to perform DBIM inversions when dealing with real data. The scanning configuration shown in Fig. 1 was simulated using two transducers. The first transducer was used as source and had a fixed position. The second transducer was used as receiver and rotated in a circular arc around the sample. Both transducers were unfocused circular pistons, with nominal center frequency of 1 MHz and reported radius of 0.0625 inches. The diameter of the transducers was chosen to be small relative to the acoustic wavelength ($ka = 6.65$ at 1 MHz) in order to generate a relatively uniform field covering the object to be imaged in both transmission and reception.

The source transducer was excited using a one-cycle sinusoidal burst at a center frequency of 1 MHz, generated by a high-power pulser/receiver (Ritec Advanced Measurement System RAM5000, Warwick, RI). The received signals were amplified by 20 dB and filtered between 300 KHz and 5 MHz using a Panametrics 5800 pulser/receiver (GE Panametrics, Waltham, MA). The overall -6 dB transmit/receive bandwidth was approximately 0.7 MHz, centered around 0.92 MHz. A GPIB-connected digital oscilloscope (LeCroy, Chestnut Ridge, NY) was used for digitization and averaging of the signals. The scans were conducted at a temperature of approximately 18.1°C .

The imaging targets were phantoms built using soft rubber balloons filled with a saline solution. The speed of sound and thickness of the balloons were estimated to be $1.54\text{ mm}/\mu\text{s}$ and 0.23 mm . These estimates were found by using pulse-echo, time-of-flight (TOF) measurements with a 20 MHz focused transducer. The saline solution was obtained by diluting 25 grams of salt in 100 milliliters of water. The speed of sound was estimated to be $1.718\text{ mm}/\mu\text{s}$ using transmission TOF measurements with the 1 MHz unfocused transducers used for inverse scattering imaging. This value agrees with results previously reported [47]. The diameter of the inflated balloon was measured to be 7.3 mm with an electronic caliper. A small metallic deadweight was attached to the bottom of the balloon phantom to keep it vertical.

The actual scanning configuration is shown in Fig. 7. The distances between the phantom and the source and receiver transducers were 104 mm and 91 mm, respectively. The receiver transducer was mounted on a vertical rod attached to an L-shaped mechanical element with adjustable horizontal length. The vertical segment of the L-shaped element was coupled to a five-axis (three translational, two rotational) precision positioning system (Daedal, Inc., Harrison City, PA). With this arrangement, rotating the vertical segment of the L-shaped element resulted in the transducer describing a circular arc around the balloon phantom, with radius given by the length of the horizontal segment. The angle between the axis of the source and receiver transducers was changed between -60 and 60 degrees in increments of 1 degree.

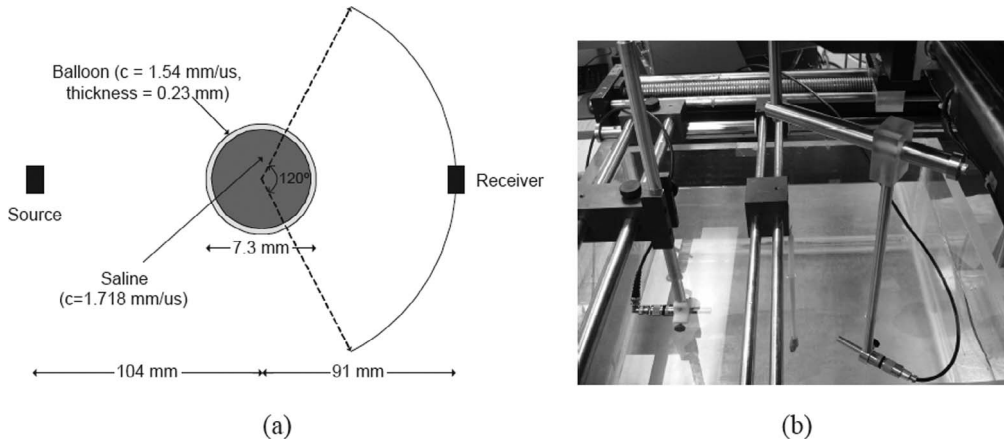


Fig. 7. Experimental configuration. (a) Schematic of the configuration setup. (b) Photograph of the experimental setup showing the source transducer (left), balloon phantom (middle), and receiver transducer attached to the rotating arm (right).

The current configuration does not allow for the transmit transducer to be rotated around the object. However, for radially symmetric phantoms like the one used in the experiments, the scattered data is independent of the incident angle if the relative positions of the transmit and receive elements remains the same. A complete dataset was generated by replicating the scattered field measured at one incident angle. The drawback of this approach is that asymmetries in the actual phantom, errors in the scattered field calculation, and noise in the measurements will propagate to all the angular views, which introduces radially symmetric artifacts.

Two sets of measurements were collected: one without the sample in the water tank to measure the incident field, and one with the sample in the tank to measure the total acoustic field in the presence of the scatterer. The scattered field is obtained by subtracting the incident field from the total field. The three fields are shown in Fig. 8 as a function of the receiving angle from -60 to 60 degrees. From Fig. 8(c), it can be observed that the incident field was not completely canceled (noticeable residual incident field of about ± 25 degrees) due to variations in the background speed of sound caused by slight variations in the temperature. However, the incident field residuals had very low amplitude and did not significantly affect the scattered field measurements.

The scattered fields at frequencies of interest were obtained by taking the Fourier transform of the measured waveforms for all receiver positions. A frequency of 1.2 MHz was chosen for the DBIM reconstructions. At this frequency, $\Delta\phi \approx 1.6\pi$ according to the phantom model and, therefore, frequency hopping was required. A lower frequency of 0.64 MHz, for which $\Delta\phi \approx 0.85\pi$, was used for the coarse reconstruction. Fig. 9 shows the measured scattered fields as a function of the receiver angle. For comparison, the ideal scattered field also was generated using the DBIM MoM forward solver. The RMSEs between the measured and expected scattered fields were 4.1% and 7.8% for 0.64 MHz and 1.2 MHz, respectively.

The phantom reconstructions are shown in Fig. 10. For comparison, the DBIM reconstruction using the scattered data generated using the MoM solver also was calculated. Both reconstructions are in very good agreement. All the reconstructions were performed using a grid with pixel size equal to 0.3075 mm (four pixels per wavelength at 1.2 MHz). The mean speed of sound and radius of the phantom were accurately reconstructed. Some minor artifacts are present in the final reconstructions (even with MoM data) due to the limited angular coverage and the small width of the balloon with respect to the wavelength. As expected, the reconstruction at 0.64 MHz had a poor spatial resolution due to the small pixel size (approximately 7.5 pixels per wavelength at that frequency), the limited angular coverage in reception, and the lack of a good initial guess. The resolution was greatly improved with the use of the frequency hopping approach, as evidenced by the reduction of the edge blurring in the reconstructed speed of sound profile. This also indicates that the proposed regularization scheme was capable of producing an accurate solution even with reduced k -space coverage, without causing an excessive blurring of the reconstruction. The RMSE in the speed of sound contrast Δc was 19% when using the 0.64 MHz experimental data only. Using the 1.2 MHz experimental data to refine the 0.64 MHz reconstruction allowed the RMSE to be reduced to 12% . The overall RMSE in the speed of sound reconstruction using the balloon model as a reference was approximately 1.1% .

V. CONCLUSIONS

Inverse scattering methods can be used to measure mechanical properties of materials, which makes them suitable for material characterization. A DBIM implementation in which the transducers are distributed on a circle surrounding the sample has been studied, and a new regularization scheme is outlined. The proper choice of regularization parameter not only allowed for high-quality re-

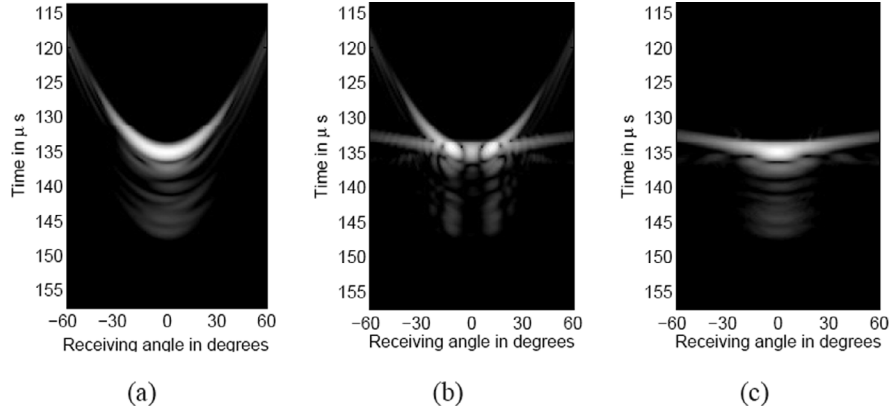


Fig. 8. Measured pressure fields in decibel scale with a dynamic range of 40 dB. (a) Incident field. (b) Total field. (c) Scattered field, calculated as the difference of (b) and (a).

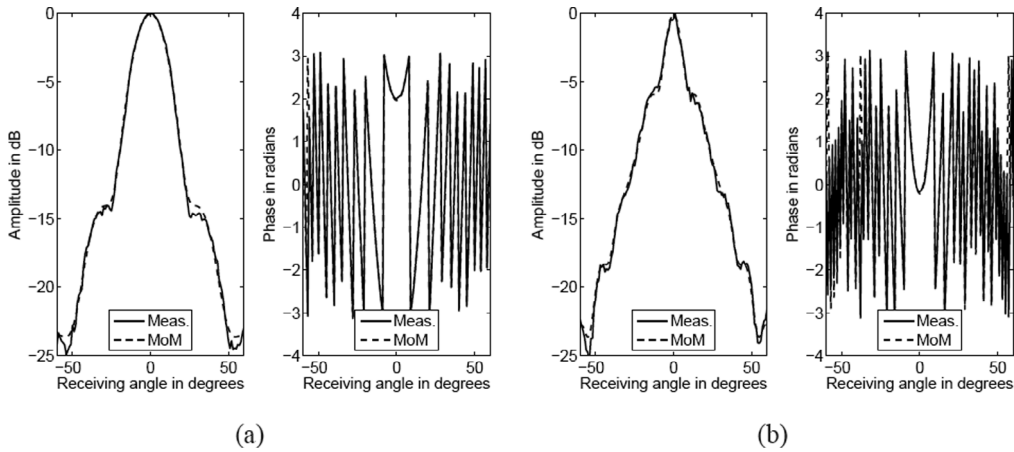


Fig. 9. Magnitude in decibels (left column) and phase in radians (right column) of the scattered pressure at (a) 0.64 MHz and (b) 1.2 MHz. Both the measured (solid line) and MoM (dashed line) data are shown.

constructions, even in the presence of noise, but also resulted in the same number of DBIM iterations regardless of spatial scaling of the imaging target while keeping $\Delta\phi$ fixed. Furthermore, by relaxing the regularization parameter with the RRE, a significant loss in spatial resolution was not observed.

The DBIM implementation and novel regularization scheme was validated using both simulation and experiments on targets with moderate Δc . Frequency hopping was used to reconstruct high resolution images of the simulated and real phantoms from coarse reconstructions made at a lower frequency. Experimental measurements from a balloon phantom with moderate Δc at 1.2 MHz, $\Delta\phi = 1.6\pi$, yielded speed of sound reconstructions with a relative RMSE of 1.1%. Therefore, the current work presents preliminary validation of the use of ultrasound-computed tomography to accurately reconstruct objects with moderate Δc .

The current work presents three contributions to the acoustic inverse scattering community. First, a computationally efficient and robust regularization approach has been developed and tested. Second, to the authors' knowledge, no other peer-reviewed article has presented exper-

imental DBIM frequency hopping results with acoustic data and nonambiguous imaging targets for which the validity of the reconstructions can be assessed. Finally, to the authors' knowledge, no other peer-reviewed article has discussed the effect of variable density in inverse scattering reconstructions using the DBIM.

APPENDIX SCATTERING OF A CYLINDRICAL WAVE BY TWO CONCENTRIC CIRCULAR CYLINDERS

The analytical solution for the acoustic field scattered by two concentric circular cylinders is derived here. A similar derivation is presented elsewhere [48] for the scattering of a plane wave by two concentric circular cylinders. The major difference between the derivation presented here and the one in [48] is that a closed-form solution to the scattering coefficients is given, as opposed to expressing the boundary conditions as a matrix equation to be solved. The corresponding radius, speed of sound, density, and wave number values are a , c_1 , ρ_1 , and k_1 for the outer cylinder, and b , c_2 , ρ_2 , and k_2 for the inner cylinder, re-

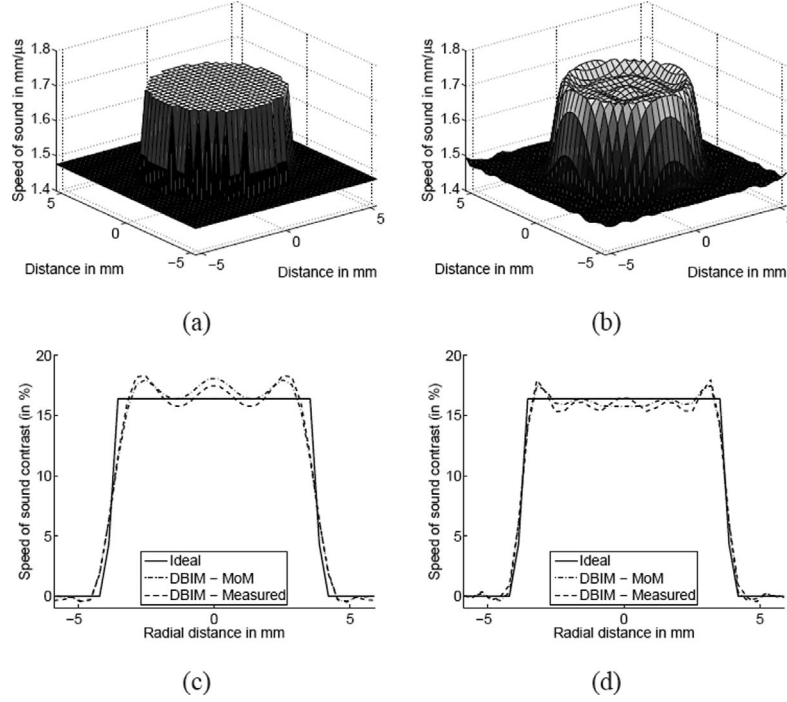


Fig. 10. DBIM reconstructions of the balloon phantom. (a) The speed of sound corresponding to the phantom model. (b) The reconstructed speed of sound profile using DBIM and measured data. (c) Profile of the reconstruction at 0.64 MHz. (d) Profile of the reconstruction at 1.2 MHz. For (c) and (d), the ideal profile according to the model (solid line) and the DBIM reconstructions using ideal (dot-dashed line) and measured (dashed line) data are shown.

spectively. The incident field is generated by a line source parallel to the z axis and can be expressed as:

$$p^{\text{inc}}(\rho, \phi) = \sum_{m=0}^{\infty} A_m H_m^{(2)}(k_0 R) J_m(k_0 \rho) \cos m\phi, \quad (9)$$

where $H_m^{(2)}(x)$ is the m -th order Hankel function of the second kind, $J_m(x)$ is the m -th order Bessel function, R is the distance from the point source to the origin, ρ is the distance from the observation point to the origin, and ϕ is the angle between source and observation points, and $A_m = 2$ if $m = 0$ or $A_m = 1$ otherwise. The scattered field can be expressed as:

$$p^{\text{sc}}(\rho, \phi) = \sum_{m=0}^{\infty} B_m H_m^{(2)}(k_0 \rho) \cos m\phi. \quad (10)$$

The field in the outer cylinder is a combination of traveling and standing waves and can be written as:

$$p^{C1}(\rho, \phi) = \sum_{m=0}^{\infty} [C_m H_m^{(2)}(k_1 \rho) + D_m J_m(k_1 \rho)] \cos m\phi, \quad (11)$$

and the field inside the inner cylinder is a standing wave and can be expanded as:

$$p^{C2}(\rho, \phi) = \sum_{m=0}^{\infty} E_m J_m(k_2 \rho) \cos m\phi. \quad (12)$$

The normal component of the particle velocity satisfies $u_r = \frac{i}{Z} \frac{\partial}{\partial k \rho} p$, where $Z = \rho c$ is the acoustic impedance.

Altogether, for each harmonic m , a matrix equation with four unknowns (B_m , C_m , D_m , and E_m) and four equations: continuity of pressure and normal particle velocity at $\rho = a$ and $\rho = b$, can be formed and solved. The coefficients B_m are of particular interest because they are the only ones needed to calculate the scattered field using (10), and are given by:

$$B_m = \left\{ \begin{aligned} & [Z_{r1} J'_m(k_1 b) J_m(k_2 b) - Z_{r2} J_m(k_1 b) J'_m(k_2 b)] \\ & \times [H_m^{(2)}(k_1 a) J'_m(k_0 a) - Z_{r1} H_m^{(2)}(k_1 a) J_m(k_0 a)] \\ & - [Z_{r1} H_m^{(2)}(k_1 b) J_m(k_2 b) - Z_{r2} H_m^{(2)}(k_1 b) J'_m(k_2 b)] \\ & \times [J_m(k_1 a) J'_m(k_0 a) - Z_{r1} J'_m(k_1 a) J_m(k_0 a)] \end{aligned} \right\} \quad (13)$$

$$\div \left\{ \begin{aligned} & [Z_{r1} H_m^{(2)}(k_1 b) J_m(k_2 b) - Z_{r2} H_m^{(2)}(k_1 b) J'_m(k_2 b)] \\ & \times [H_m^{(2)}(k_0 a) J_m(k_1 a) - Z_{r1} H_m^{(2)}(k_0 a) J'_m(k_1 a)] \\ & - [Z_{r1} J'_m(k_1 b) J_m(k_2 b) - Z_{r2} J_m(k_1 b) J'_m(k_2 b)] \\ & \times [H_m^{(2)}(k_0 a) H_m^{(2)}(k_1 a) - Z_{r1} H_m^{(2)}(k_0 a) H_m^{(2)}(k_1 a)] \end{aligned} \right\},$$

$$A_m H_m^{(2)}(k_0 R),$$

where $Z_{r1} = Z_0/Z_1$, $Z_{r2} = Z_0/Z_2$, and the prime symbol in the Bessel and Hankel functions denote the derivative with respect to the total argument. For the special case when the inner and outer cylinders are matched (i.e., $k_1 = k_2 = k$, $Z_{r1} = Z_{r2} = Z_r$), the scattering coefficients from (13) can be simplified to:

$$B_m = -A_m [J_m(ka)J'_m(k_0a) - Z_r J_m(k_0a)J'_m(ka)] \\ \div [J_m(ka)H_m^{(2)}(k_0a) - Z_r J'_m(ka)H_m^{(2)}(k_0a)] H_m^{(2)}(k_0R), \quad (14)$$

which corresponds to the scattering of a cylindrical wave by a homogeneous fluid circular cylinder [43].

ACKNOWLEDGMENTS

The authors would like to thank Dr. W. C. Chew and A. Hesford for many useful discussions about the DBIM; Dr. W. D. O'Brien, Jr., for his suggestions about the experimental work; and Dr. S. Bond for discussions on the computational implementation of DBIM.

REFERENCES

- [1] C. F. Schueler, H. Lee, and G. Wade, "Fundamentals of digital ultrasonic processing," *IEEE Trans. Sonics Ultrason.*, vol. 31, pp. 195–217, July 1984.
- [2] A. Macovski, "Ultrasonic imaging using arrays," *Proc. IEEE*, vol. 67, pp. 484–495, Apr. 1979.
- [3] Q. Zhu and B. D. Steinberg, "Wavefront amplitude distortion and image sidelobe levels: Part I—Theory and computer simulations," *IEEE Trans. Ultrason., Ferroelect., Freq. Contr.*, vol. 40, no. 6, pp. 747–753, Nov. 1993.
- [4] A. Kak and M. Slaney, *Principles of Computerized Tomographic Imaging*. Philadelphia, PA: SIAM, 2001.
- [5] J. Greenleaf, J. Ylitalo, and J. Gisvold, "Ultrasonic computed tomography for breast examination," *IEEE Eng. Med. Biol. Mag.*, vol. 6, pp. 27–32, Dec. 1987.
- [6] M. P. Andre, H. S. Janeé, P. J. Martin, G. P. Otto, B. A. Spivey, and D. A. Palmer, "High-speed data acquisition in a diffraction tomography system employing large-scale toroidal arrays," *Int. J. Imag. Syst. Technol.*, vol. 8, no. 1, pp. 137–147, 1997.
- [7] J. Wiskin, D. Borup, S. Johnson, M. Berggren, T. Abbott, and R. Hanover, "Full wave, non-linear, inverse scattering," *Acoust. Imag.*, vol. 28, pp. 183–194, 2007.
- [8] S. A. Johnson, T. Abbott, R. Bell, M. Berggren, D. Borup, D. Robinson, J. Wiskin, S. Olsen, and B. Hanover, "Noninvasive breast tissue characterization using ultrasound speed and attenuation," *Acoust. Imag.*, vol. 28, pp. 147–154, 2007.
- [9] N. Duric, P. Littrup, A. Babkin, D. Chambers, S. Azevedo, A. Kalinin, R. Pevzner, M. Tokarev, E. Holsapple, O. Rama, and R. Duncan, "Development of ultrasound tomography for breast imaging: Technical assessment," *Med. Phys.*, vol. 32, pp. 1375–1386, May 2005.
- [10] P. D. Edmonds, C. L. Mortensen, J. R. Hill, S. K. Holland, J. F. Jensen, P. Schattner, A. D. Valdes, R. H. Lee, and F. A. Marzoni, "Ultrasound tissue characterization of breast biopsy specimens," *Ultrason. Imag.*, vol. 13, pp. 162–185, Apr. 1991.
- [11] X. Zhang, S. Broschat, and P. Flynn, "A comparison of material classification techniques for ultrasound inverse imaging," *J. Acoust. Soc. Amer.*, vol. 111, pp. 457–467, Jan. 2002.
- [12] A. Abubakar, T. M. Habashy, P. M. van den Berg, and D. Gisolf, "The diagonalized contrast source approach: An inversion method beyond the Born approximation," *Inverse Problems*, vol. 21, pp. 685–702, Apr. 2005.
- [13] J. Greenleaf, S. Johnson, W. Samayoa, and F. Duck, "Algebraic reconstruction of spatial distributions of acoustic velocities in tissue from their time-of-flight profiles," *Acoust. Hologr.*, vol. 6, pp. 71–90, 1975.
- [14] J. Greenleaf, S. Johnson, S. Lee, G. Herman, and E. Wood, "Algebraic reconstruction of spatial distributions of acoustic absorption within tissue from their two-dimensional acoustic projections," *Acoust. Hologr.*, vol. 5, pp. 591–603, 1974.
- [15] A. Devaney, "Inversion formula for inverse scattering within the Born approximation," *Opt. Lett.*, vol. 7, pp. 111–112, Mar. 1982.
- [16] A. Devaney, "Inverse-scattering theory within the Rytov approximation," *Opt. Lett.*, vol. 6, pp. 374–376, Aug. 1981.
- [17] M. Slaney, A. Kak, and L. Larsen, "Limitations of imaging with first-order diffraction tomography," *IEEE Trans. Microwave Theory Tech.*, vol. 32, pp. 860–874, Aug. 1984.
- [18] B. Robinson and J. Greenleaf, "The scattering of ultrasound by cylinders: Implications for diffraction tomography," *J. Acoust. Soc. Amer.*, vol. 80, pp. 40–49, July 1986.
- [19] W. C. Chew and Y. M. Wang, "Reconstruction of two-dimensional permittivity distribution using the distorted Born iterative method," *IEEE Trans. Med. Imag.*, vol. 9, pp. 218–225, June 1990.
- [20] D. Borup, S. Johnson, W. Kim, and M. Berggren, "Nonperturbative diffraction tomography via Gauss-Newton iteration applied to the scattering integral equation," *Ultrason. Imag.*, vol. 14, pp. 69–85, Jan. 1992.
- [21] T. Cavicchi, S. Johnson, and W. D. O'Brien, Jr., "Application of the sinc basis moment method to the reconstruction of infinite circular cylinders," *IEEE Trans. Ultrason., Ferroelect., Freq. Contr.*, vol. 35, pp. 22–33, Jan. 1988.
- [22] W. C. Chew and J. H. Lin, "A frequency-hopping approach for microwave imaging of large inhomogeneous bodies," *IEEE Microwave Guided Wave Lett.*, vol. 5, pp. 440–441, Dec. 1995.
- [23] F. Natterer, "An algorithm for the fully nonlinear inverse scattering problem at fixed frequency," *J. Comput. Acoust.*, vol. 9, pp. 935–940, Sep. 2001.
- [24] F. Natterer and F. Wubelling, "Marching schemes for inverse acoustic scattering problems," *Numerische Mathematik*, vol. 100, pp. 697–710, June 2005.
- [25] J. Wiskin, D. Borup, and S. Johnson, "Inverse scattering from arbitrary two-dimensional objects in stratified environments via a Green's operator," *J. Acoust. Soc. Amer.*, vol. 102, pp. 853–864, Aug. 1997.
- [26] M. Tracy and S. Johnson, "Inverse scattering solutions by a sinc basis, multiple source, moment method—Part II: Numerical evaluations," *Ultrason. Imag.*, vol. 5, pp. 376–392, Oct. 1983.
- [27] H. A. Van der Vorst, "Bi-CGSTAB: A fast and smoothly converging variant of Bi-CG for the solution of nonsymmetric linear systems," *SIAM J. Sci. Stat. Comput.*, vol. 13, pp. 631–644, Mar. 1992.
- [28] D. T. Borup and O. P. Ghandi, "Fast Fourier transform method for calculation of SAR distributions in finely discretized inhomogeneous models of biological bodies," *IEEE Trans. Microwave Theory Tech.*, vol. 32, pp. 355–360, Apr. 1984.
- [29] T. J. Cui, W. C. Chew, A. A. Aydinler, and S. Cheng, "Inverse scattering of two-dimensional dielectric objects buried in a lossy earth using the distorted Born iterative method," *IEEE Trans. Geosci. Remote Sens.*, vol. 39, pp. 339–346, Feb. 2001.
- [30] W. H. Weedon and W. C. Chew, "Time-domain inverse scattering using the local shape function (LSF) method," *Inverse Problems*, vol. 9, pp. 551–564, Oct. 1993.
- [31] A. J. Hesford and W. C. Chew, "A frequency-domain formulation of the Fréchet derivative to exploit the inherent parallelism of the distorted Born iterative method," *Waves Random Complex Media*, vol. 16, pp. 495–508, Nov. 2006.
- [32] O. Haddadin and E. Ebbini, "Imaging strongly scattering media using a multiple frequency distorted Born iterative method," *IEEE Trans. Ultrason., Ferroelect., Freq. Contr.*, vol. 45, pp. 1485–1496, Nov. 1998.
- [33] C. R. Vogel, *Computational Methods for Inverse Problems*. Philadelphia, PA: SIAM, 2002.
- [34] P. C. Hansen, "Analysis of discrete ill-posed problems by means of the L-curve," *SIAM Rev.*, vol. 34, pp. 561–580, Dec. 1992.
- [35] G. H. Golub, M. Heath, and G. Wahba, "Generalized cross-validation as a method for choosing a good ridge parameter," *Technometrics*, vol. 21, pp. 215–223, 1979.
- [36] J. L. Castellanos, S. Gomez, and V. Guerra, "The triangle method for finding the corner of the L-curve," *Appl. Numer. Math.*, vol. 43, pp. 359–373, Dec. 2002.
- [37] O. S. Haddadin and E. S. Ebbini, "Adaptive regularization of a distorted Born iterative algorithm for diffraction tomography," in *Proc. IEEE Int. Conf. Image Processing*, 1996, pp. 725–728.
- [38] Q. H. Liu, "Reconstruction of two-dimensional axisymmetric inhomogeneous media," *IEEE Trans. Geosci. Remote Sens.*, vol. 31, pp. 587–594, May 1993.

- [39] A. Franchois and C. Pichot, "Microwave imaging—Complex permittivity reconstruction with a Levenberg-Marquardt method," *IEEE Trans. Antennas Propagat.*, vol. 45, pp. 203–215, Feb. 1997.
- [40] G. L. Wang, W. C. Chew, T. J. Cui, A. A. Aydinler, D. L. Wright, and D. V. Smith, "3D near-to-surface conductivity reconstruction by inversion of VETEM data using the distorted Born iterative method," *Inverse Problems*, vol. 20, pp. 195–216, Dec. 2004.
- [41] T. J. Cui, W. C. Chew, X. X. Yin, and W. Hong, "Study of resolution and super resolution in electromagnetic imaging for half-space problems," *IEEE Trans. Antennas Propagat.*, vol. 52, pp. 1398–1411, June 2004.
- [42] M. T. Heath, *Scientific Computing: An Introductory Survey*. New York: McGraw-Hill, 2002.
- [43] T. Cavicchi and W. D. O'Brien, Jr., "Acoustic scattering of an incident cylindrical wave by an infinite circular cylinder," *IEEE Trans. Ultrason., Ferroelect., Freq. Contr.*, vol. 35, pp. 78–80, Jan. 1988.
- [44] S. A. Johnson and F. Stenger, "Ultrasound tomography by Galerkin or moment methods," in *Lecture Notes in Medical Informatics*, vol. 23, ser. Selected Topics in Image Science, O. Nalcioglu and Z. Cho, Eds. New York, NY: Springer-Verlag, 1984, pp. 254–275.
- [45] J. Lin and W. Chew, "Ultrasonic imaging by local shape function method with CGFFT," *IEEE Trans. Ultrason., Ferroelect., Freq. Contr.*, vol. 43, pp. 956–969, Sep. 1996.
- [46] S.-J. Kwon and M.-K. Jeong, "Ultrasound inverse scattering determination of speed of sound, density, and absorption," in *Proc. IEEE Ultrason. Symp.*, 1998, pp. 1631–1634.
- [47] C. A. Edwards and W. D. O'Brien, Jr., "Speed of sound in mammalian tendon threads using various reference media," *IEEE Trans. Sonics Ultrason.*, vol. 32, pp. 351–354, Mar. 1985.
- [48] J. Sinai and R. C. Waag, "Ultrasonic scattering by two concentric cylinders," *J. Acoust. Soc. Amer.*, vol. 83, pp. 1728–1735, May 1988.



Roberto Lavarello was born in Lima, Peru in 1978. He earned his B.S. degree in electrical engineering in 2000 from the Pontificia Universidad Catolica del Peru, Lima, Peru, and his M.S. degree in electrical and computer engineering in 2005 from the University of Illinois at Urbana-Champaign, where he is currently pursuing the Ph.D. degree. Mr. Lavarello was a Fulbright Scholarship recipient from 2003 to 2005. His research interests include ultrasonic imaging, computational methods for acoustic propagation, and inverse problems with emphasis on acoustical inverse scattering. He is a student member of IEEE and IEEE UFFC.



Michael Oelze was born in Hamilton, New Zealand in 1971. He earned his B.S. degree in physics and mathematics in 1994 from Harding University, Searcy, AR, his M.S. degree in physics in 1996 from the University of Louisiana at Lafayette, Lafayette, LA, and his Ph.D. degree in physics in 2000 from the University of Mississippi, Oxford, MS. Dr. Oelze was a post-doctoral fellow at the University of Illinois at Urbana-Champaign from 2000 to 2004 conducting research in ultrasound. His research interests include the acoustic interaction with soil, ultrasound tissue characterization, quantitative ultrasound, ultrasound bioeffects, ultrasound tomography techniques, and application of coded excitation to ultrasound imaging. Currently, Dr. Oelze is an assistant professor at the University of Illinois at Urbana-Champaign. Dr. Oelze is a member of the IEEE, IEEE UFFC, AIUM, and ASA.